

Improving Autoregressive Visual Generation with Cluster-Oriented Token Prediction

Teng Hu¹, Jiangning Zhang^{2,3*}, Ran Yi^{1†}, Jieyu Weng¹, Yabiao Wang^{2,3},
 Xianfang Zeng³, Zhucun Xue³, Lizhuang Ma¹
¹Shanghai Jiao Tong University, ²Youtu Lab, Tencent, ³Zhejiang University
 {hu-teng, ranyi}@sjtu.edu.cn, vtzhang@tencent.com
 Code: <https://github.com/sjtuplayer/IAR>

Abstract

Employing LLMs for visual generation has recently become a research focus. However, the existing methods primarily transfer the LLM architecture to visual generation but rarely investigate the fundamental differences between language and vision. This oversight may lead to suboptimal utilization of visual generation capabilities within the LLM framework. In this paper, we explore the characteristics of visual embedding space under the LLM framework and discover that the correlation between visual embeddings can help achieve more stable and robust generation results. We present **IAR**, an **Improved AutoRegressive Visual Generation Method** that enhances the training efficiency and generation quality of LLM-based visual generation models. Firstly, we propose a **Codebook Rearrangement** strategy that uses balanced k -means clustering algorithm to rearrange the visual codebook into clusters, ensuring high similarity among visual features within each cluster. Leveraging the rearranged codebook, we propose a **Cluster-oriented Cross-entropy Loss** that guides the model to correctly predict the cluster where the target token is located. This approach ensures that even if the model predicts the wrong token index, there is a high probability the predicted token is located in the correct cluster, which significantly enhances the generation quality and robustness. Extensive experiments demonstrate that our IAR consistently enhances the model training efficiency and performance from 100M to 1.4B, reducing the training time by half while achieving the same FID. Additionally, IAR can be applied to various LLM-based visual generation models and adheres to the scaling law, providing a promising direction for future research in LLM-based visual generation.

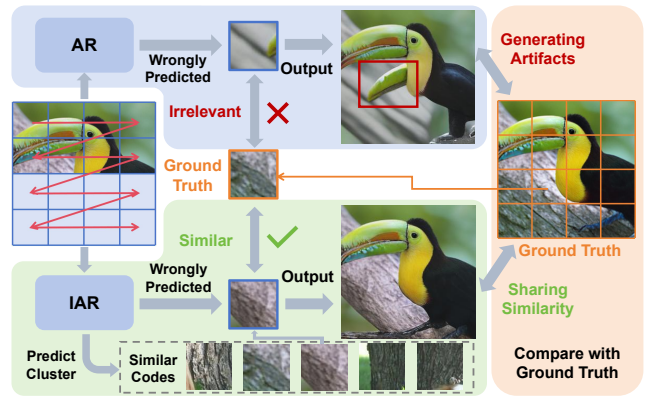


Figure 1. When an autoregressive model predicts a wrong token, the previous methods [38, 40] may predict an irrelevant token that causes artifacts. Our IAR alleviates this issue by ensuring a high probability of the predicted token located in the correct cluster.

1. Introduction

With the development of generative models [16, 20, 35], a large number of outstanding visual generation methods have emerged, achieving considerable success in image and video generation [4, 17, 35]. Recently, researchers have begun exploring the integration of images and text to achieve a unified multi-modal model for image and text generation and understanding [39, 45]. Consequently, aligning image generation models with large language models (LLMs) [34] has become a key research focus. Recent studies have made progress by quantizing images and employing autoregressive or mask-prediction methods to predict discrete image tokens [3, 7, 38, 40], laying the research foundation for a unified world model in the future.

Unlike diffusion [20] or GAN [16] models that model image distribution in continuous space, autoregressive or masked image modeling (MIM) methods [3, 7, 38, 40] first convert images into discrete-valued tokens by image tokenizers, and then predict image tokens by autoregressive or

*Project leader.

†Corresponding author.

MIM approach. Specifically, autoregressive methods use the “next-token prediction” paradigm of GPT [34], while MIM methods adopt a similar training strategy to the mask prediction in BERT [12]. These methods draw inspiration from natural language models and transfer these techniques to image generation models, but rarely explore the fundamental differences between images and natural language.

Due to the inherently discrete nature of words (each word comes from a finite vocabulary), different words can be directly mapped to different indices through a lookup table, thereby generating text by predicting the corresponding index of the target text. The standard language modeling objective $p(x_t|x_1, \dots, x_{t-1})$ (each x_t is an index) then can be interpreted as a classification task and accurately modeled by LLMs. However, images are continuous-valued, and if the same objective is applied to image generation with x_t as a real number, it is difficult to accurately model this probability density. Therefore, image tokenizers such as VQGAN [14] are used to convert continuous images into discrete-valued tokens, and then the model predicts the image token index. Afterwards, the corresponding image embedding is retrieved from the codebook and decoded into an image. A fundamental difference between image and text is that, in text generation, the predicted text index can be directly mapped to the corresponding word through a lookup table; whereas LLM-based image generation essentially requires the image embedding that corresponds to the index, and then decodes it into an image. *I.e.*, text only requires the index, while image requires the embedding corresponding to the index.

Different from the token index which is independent, *i.e.*, the nearby indices have no correlation in word semantics, the image embeddings are located in a continuous feature space, where similar embeddings may correspond to similar image contents. This paper first investigates the impact of image embedding correlations on the generated results, and finds that *similar embeddings convey similar information in the image space*: When the embeddings of certain image patches are replaced by similar image embeddings, the decoded images are nearly identical. This insight inspires us to leverage the similarity of image embeddings to improve the existing LLM-based image generation techniques.

To capitalize on the correlation among image embeddings, we propose **IAR**, an **Improved AutoRegressive Visual Generation Method**, which can enhance the training efficiency and generation quality of the LLM-based visual generation model. Firstly, we propose a **Codebook Rearrangement** strategy that uses balanced K-means clustering algorithm to rearrange the embeddings in the codebook into clusters of equal sizes, where the embeddings in each cluster share high similarities and can be decoded into images with similar contents. Secondly, we observe that if a token index is wrongly predicted as a similar embedding’s

index, the original token-oriented cross-entropy loss used in LLM will penalize this case, but the decoded image is actually not much different from the target image. To tolerate this case, based on the rearranged codebook, we further introduce a **Cluster-oriented Cross-entropy Loss**, which guides the model to predict the correct cluster that contains the target token, thereby providing the model with a broader perspective and no longer confined to a single target token. Combined with the original token-oriented cross-entropy loss, our model can consider both the target cluster and the target token. Even if the model predicts the wrong token index, with our rearranged codebook and cluster-oriented loss, there is a high probability that the token is located in the target cluster, which ensures a high similarity between the output image and the target one, effectively improving the generation quality and robustness (Fig. 1).

We develop our model based on LlamaGen [38] and compare with existing visual generation methods based on GAN, Diffusion, Autoregressive (AR), and MIM models. Extensive experiments demonstrate that, across different parameter scales of LlamaGen (ranging from 100M to 1.4B), our method consistently enhances the model’s training efficiency and performance. For the same FID, our approach reduces LlamaGen’s training time by half, and under the same number of training epochs, it effectively improves the model’s generation quality. Our method can be applied to various LLM-based visual generation models with almost no additional training costs, and adheres to the scaling law, providing a promising direction for improving future LLM-based visual generation models.

Our main contributions can be summarized as four-fold:

- We propose **IAR**, an Improved Autoregressive Visual Generation method, which leverages the correlation of visual embeddings to enhance the training efficiency and performance of LLM-based visual generation models.
- We introduce a **Codebook Rearrangement** strategy that uses balanced K-means clustering algorithm to rearrange the image codebook, ensuring high similarity across image embeddings within each cluster.
- We propose a **Cluster-oriented Cross-entropy Loss** that relaxes the original token-oriented cross-entropy, ensuring that even if the model predicts the wrong token index, there is still a high probability that the token is in the correct cluster, thereby generating high-quality images.
- Extensive experiments demonstrate the effectiveness of our method. Additionally, our approach can be applied to various LLM-based visual generation models, adheres to the scaling law, and provides a robust improvement direction for future LLM-based visual generation models.

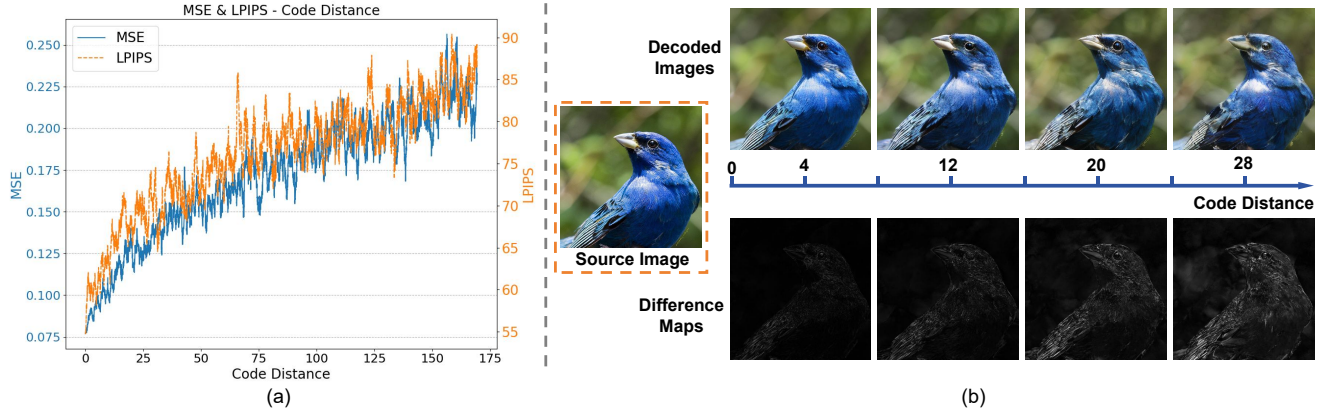


Figure 2. (a) The MSE and LPIPS between the source image and the decoded image with different code distances. (b) The visualization of the images decoded from different code distances. When the code distance is within a certain range (e.g., smaller than 12), the decoded image looks nearly identical to the source image. We further make use of this property to improve the LLM-based visual generation model.

2. Related Works

2.1. Large language models

Large language models (LLMs) [12, 34, 41] have achieved significant success in natural language processing (NLP). The encoder-only structure [10, 12, 28], exemplified by BERT [12], randomly masks portions of the text and predicts the masked tokens based on the unmasked ones. With the introduction of the GPT series [1, 6, 33, 34], the decoder-only architecture gained popularity, demonstrating remarkable capabilities in language processing through next-token prediction. Additionally, open-source models such as LLaMA [30] and PaLM [9] have further advanced the NLP field. The recent success of LLMs in natural language processing has also inspired researchers to apply these models to visual generation, revealing significant potential in multi-modal generation tasks.

2.2. Visual Generation Models

Continuous-valued Visual Generation. Generative Adversarial Networks (GANs) [14, 16, 25, 43], consisting of a generator and discriminator, employ adversarial training to learn the target distribution. Diffusion Models [13, 15, 20, 21, 31, 35] iteratively add and remove noise to approximate the real data distribution, using a Markov process for the forward path and learning the reverse denoising process. These models have achieved significant success in image generation and have been extended to video generation [4, 17, 42], enhancing video quality. However, both GANs and Diffusion Models, which model continuous distributions, face challenges when integrating with discretely modeled LLMs. Thus, exploring discrete modeling methods for image generation is necessary.

Discrete-valued Visual Generation. Discrete-space visual generation models are mainly divided into autoregressive [14, 38, 40] and masked image modeling (MIM) [3, 7,

8] models, both requiring image quantization before generation. Autoregressive models follow the next-token generation approach of GPT [1, 34], predicting subsequent tokens one by one based on previous image tokens. LLaM-AGEN [38], a representative work, uses LLAMA [41] to model the image generation process. VAR [40] further enhances generation capability by proposing a next-scale image generation process. MIM methods [3, 7, 38, 40], inspired by BERT [12], randomly mask parts of the image tokens and predict the masked tokens using the unmasked ones. These methods directly draw inspiration from LLMs and rarely explore the fundamental differences between images and language, which may lead to suboptimal utilization of vision generation capabilities within the LLM framework. In contrast, our model makes full use of the image property, which effectively improves the training efficiency and model performance in LLM-based image generation.

3. Method

Observing that an inherent difference between LLM-based image generation and text generation lies in that text generation only requires a predicted text index that can be directly mapped into the corresponding word, while image generation essentially requires the image embedding that corresponds to the index, and then decodes it into an image, we further explore the characteristics of the image embedding space. We conduct a detailed analysis on the similarity of the image embeddings in the codebook learned by image tokenizers (Sec. 3), and find that similar embeddings convey similar information in the image space: When the embeddings of certain image patches are replaced by similar image embeddings, the decoded images are nearly identical. Therefore, we leverage this property to enhance the LLM-based image generation model.

We first propose a **Codebook Rearrangement** strategy

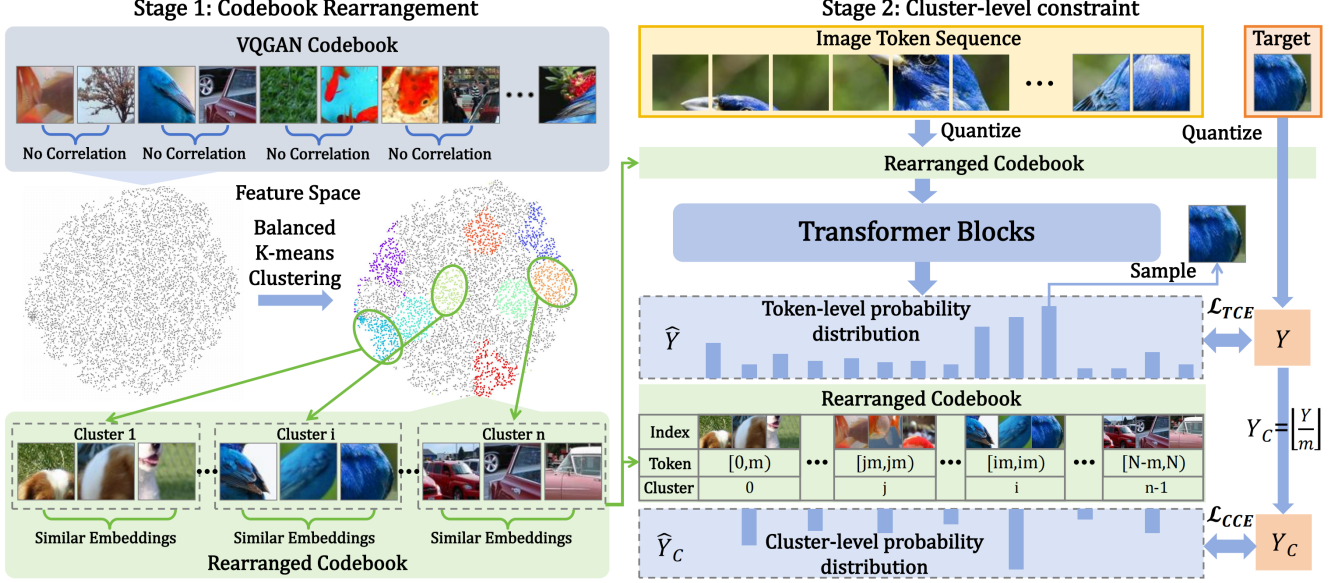


Figure 3. Model framework: 1) **Codebook Rearrangement**: we first use a balanced K-means clustering method to rearrange the codebook, which divides the codebook into n clusters, with the image codes in each cluster sharing a high similarity. 2) **Cluster-oriented Constraint**: During the training process, we first quantize the image patches using the rearranged codebook. For the output probability distribution \hat{Y} , we further compute the cluster-level distribution Y_C by applying LogSumExp operation for the probabilities in each cluster $\hat{Y}_{j m} \sim \hat{Y}_{(j+1)m-1}$. Then we compute the cluster-oriented cross-entropy loss \mathcal{L}_{CCE} apart from the token-oriented cross-entropy loss \mathcal{L}_{TCE} , which ensures a high probability of the predicted token located in the correct cluster, thereby enhancing generation quality.

that uses a balanced K-means clustering method to rearrange the embeddings in the codebook into clusters of equal sizes (Fig. 3 (left), Sec. 3.2), where the image embeddings in each cluster share a high similarity. Once the model predicts the correct cluster index (even if the token index is wrong), the corresponding embedding is located in the correct cluster and is thus similar to the target one, then the output images will be quite similar to the target image. To enable the model with the ability to predict the correct cluster index, we further propose a **Cluster-oriented Cross-entropy Loss** (Fig. 3 (right), Sec. 3.3). Our rearranged codebook and cluster-oriented cross-entropy loss ensure that, even if the model predicts incorrect tokens, there is a high probability of correctly predicting the cluster indices, which ensures high-quality generation results, largely improving the training efficiency and robustness of the LLM-based image generation model.

3.1. Analysis on Image Embedding Similarity

We first analyze the similarity of image embeddings in the codebook learned by image tokenizers, and find that similar embeddings (those that are close in distance) represent similar image information. *I.e.*, when the embeddings of each image patch are replaced by other similar embeddings, the content of the decoded image remains almost unchanged. To verify this image embedding similarity property, we conduct detailed experiments on the codebook of

VQGAN [14].

Specifically, an image x is quantized into discrete tokens by: 1) using an image encoder E (*e.g.*, from VQGAN [14]) to extract features, obtaining $h \times w$ image features of dimension C , denoted as $\hat{z} = E(x) \in \mathcal{R}^{h \times w \times C}$; 2) quantizing each feature $\hat{z}^{(i,j)}$ into the code index $q^{(i,j)}$ of the nearest code in the codebook $\mathcal{Z} \in \mathcal{R}^{N \times C}$:

$$q^{(i,j)} = \arg \min_{z_k \in \mathcal{Z}} \|\hat{z}^{(i,j)} - z_k\| \in [0, N), \quad (1)$$

where z_k is the k -th embedding in codebook \mathcal{Z} , and $\|\cdot\|$ measures the Euclidean distance. And the quantized feature $z_q \in \mathcal{R}^{h \times w \times C}$ is obtained by looking up each $q^{(i,j)}$ in \mathcal{Z} .

To measure the distance between two embeddings z_i, z_j in the codebook, we define the “code distance” $D(z_i, z_j)$:

$$D(z_i, z_j) := d, \quad z_j = [\text{sort}(\{\|z_k - z_i\|\})]_d, \quad (2)$$

calculated by measuring the Euclidean distance of each z_k to z_i , sorting the distances, and z_j is the $D(z_i, z_j)$ -th closest embedding to z_i among all embeddings in the codebook. A lower “code distance” indicates the two embeddings are closer in the embedding space.

Given an input image x , the quantized embedding z_q , and a generated image $\hat{x}' = G(z'_q)$ decoded from z'_q , we evaluate the similarity of the two images at different code distances $D(z_q, z'_q)$. In Fig. 2 (a), we measure the image similarity by MSE distance and LPIPS [44], where lower

Algorithm 1 Balanced k-means Clustering

Input: Codebook \mathcal{Z} , number of clusters n **Output:** The rearranged codebook $\hat{\mathcal{Z}}$ with local similarity

```
1: Initialize:
2:   Compute the cluster size  $m \leftarrow \lfloor |\mathcal{Z}|/n \rfloor$ 
3:   Randomly select  $n$  codes as initial centroids  $\{c_j\}_{j=1}^n$ 
4:   Initialize iteration counter  $iter \leftarrow 0$ 
5: repeat
6:   Compute the minimum distance  $d_i$  from  $z_i$  to  $\{c_j\}_{j=1}^n$ 
7:   Sort  $\{z_i\}$  in ascending order of  $d_i$  to form  $\mathcal{Z}'$ 
8:   for each data point  $z_i \in \mathcal{Z}'$  do
9:     Compute the distance from  $z_i$  to each centroid  $c_j$ 
10:    Assign  $z_i$  to the nearest cluster whose size does not
        exceed  $m$ 
11:   end for
12:   for each cluster centroid  $c_j$  do
13:     Update  $c_j$  to the average of all embeddings assigned
        to cluster  $j$ 
14:   end for
15:   Increment iteration counter  $iter \leftarrow iter + 1$ 
16: until convergence or reaching  $max\_iters$ 
17: for each cluster centroid  $c_j$  do
18:   Assign the embeddings in cluster  $j$  to  $\hat{\mathcal{Z}}_{[jm, (j+1)m]}$ 
19: end for
20: return The rearranged codebook  $\hat{\mathcal{Z}}$ 
```

scores indicate higher image similarity. Results show: 1) as the code distance increases, the image distance also increases; 2) but when the code distance is within a certain range (e.g., smaller than 12), the image distance (MSE 0.104 and LPIPS 66.44) does not increase too much compared to the reconstructed image $G(z_q)$ (whose code distance is 0 and has a 0.076 MSE and 55.8 LPIPS). We further visualize the images decoded from different code distances in Fig. 2(b), which shows the decoded images with lower code distances (e.g., smaller than 12) look nearly identical to the source image and have a good visual quality. This indicates that even if the predicted token index is not the accurate target index, as long as the code distance between the corresponding embedding is within a certain range, the decoded image is similar to the desired one and shows a good visual quality. Therefore, we make use of this property to improve the generation quality and stability of the LLM-based visual generation model.

3.2. Codebook Rearrangement

Rearrangement Target. In a codebook learned from the VQGAN [14] training process, the embeddings are often randomly distributed, with adjacent embeddings having no particular correlation, i.e., Euclidean distances between adjacent embeddings can be either close or far. Therefore, we first propose a Codebook Rearrangement strategy to reorder the codebook, so that the similarity between adjacent embeddings is maximized, ensuring that the surrounding em-

beddings of any given embedding exhibit high similarity.

Specifically, denote the codebook as $\mathcal{Z} = \{z_i\}_{i=1}^N$, which contains N quantized embeddings z_i . To maximize the similarity between the adjacent embeddings, we aim to find a surjective mapping $M(\cdot)$ that satisfies:

$$M = \arg \min_M \sum_{i=1}^{N-1} \|z_{M(i)}, z_{M(i+1)}\|. \quad (3)$$

I.e., after reordering each embedding z_i to index $M(i)$, the sum of distances between adjacent embeddings is minimized. And $\hat{\mathcal{Z}} = M(\mathcal{Z})$ is the rearranged codebook.

However, this optimization can be reduced to the Hamiltonian path problem (see #Suppl), and solving such a problem is NP-hard. Therefore, we try to relax this problem into a solvable form.

Constraint Relaxation. We relax this optimization problem into a much easier one, where we only need to ensure the embeddings in a range are similar. Therefore, we split the codebook into n clusters, with each cluster containing $m = \frac{N}{n}$ embeddings that are similar to each other. Then we reorder the codebook so that the embeddings in the same cluster have close indices, with the indices of cluster j are within the range $[jm, (j+1)m)$.

Balanced K-means Clustering. To cluster the embeddings in the codebook, we design a balanced K-means clustering method to uniformly divide the codebook into n clusters, with the embeddings in each cluster close to each other.

As shown in Alg. 1, we first randomly select n codes as the initial centroids $\{c_j\}_{j=1}^n$. Then, we iteratively update each cluster. In each iteration, 1) we first compute the minimum distance d_i from each embedding z_i to the n centroids $\{c_j\}_{j=1}^n$. 2) We sort $\{z_i\}$ in ascending order of d_i to form \mathcal{Z}' (i.e., embeddings closer to the nearest centroid has smaller index). This sorting and reordering step ensures that the embeddings closer to the nearest centroid are allocated first, and the farther ones are allocated later, which is necessary in cluster size balanced clustering. 3) Then, for each z_i in the ordered codebook \mathcal{Z}' , we compute its distance to each centroid c_j . 4) We assign z_i to the nearest cluster whose size does not exceed m (where $m = \frac{N}{n}$). 5) Finally, we update each cluster centroid c_j to the average of the embeddings assigned to that cluster, and repeat the above process until it converges or reaches the pre-defined maximum iteration. After obtaining the final cluster centroids c_j and n clusters, where each cluster contains m embeddings, we rearrange the codebook $\hat{\mathcal{Z}}$ by assigning the embeddings in cluster j to indices $[jm, (j+1)m)$.

3.3. Cluster-oriented Visual Generation

Analysis on Token-oriented Cross-entropy Loss. In LLM-based visual generation models [38, 40], cross-entropy loss is the most commonly used loss in the training

process. Denote the ground truth one-hot vector as Y (Y is a N -dimensional vector, with $Y_{i=y} = 1$ and $Y_{i \neq y} = 0$, where y is the class label of the token), and the predicted probability distribution as $\hat{Y} \in \mathcal{R}^N$ ($\sum \hat{Y}_i = 1$). The token-oriented cross-entropy loss \mathcal{L}_{TCE} is formulated as:

$$\mathcal{L}_{TCE} = - \sum_{i=1}^n Y_i \log \hat{Y}_i. \quad (4)$$

However, we observe that if a token index is wrongly predicted as a similar embedding’s index, this token-oriented cross-entropy loss will penalize the case, but the decoded image is actually not much different from the target image.

To tolerate this case, we leverage the rearranged codebook, where the embeddings in the same cluster are close to each other. In Sec. 3, it has been demonstrated that even if some image token indices are predicted incorrectly, as long as the embeddings of the predicted tokens are not far from the embeddings of the target tokens, the semantic integrity and quality of the generated image will not be significantly affected. Therefore, leveraging the reordered codebook from Sec. 3.2, a natural idea is to guide the model to first predict the cluster and then locate the specific token within that cluster. Since the number of clusters (n) is much smaller than the size of the codebook (N), predicting the cluster of a token is a much easier task than directly predicting a specific token. Once the cluster is accurately predicted, even if the specific token prediction is incorrect, the quality of the generated image can still be maintained.

Cluster-oriented Cross-entropy Loss. To guide the model to predict the correct cluster of the next token, we propose a cluster-wise cross-entropy loss \mathcal{L}_C . Specifically, we first derive the ground truth cluster label y_c from the class label y^1 by $y_c = \lfloor \frac{y}{m} \rfloor$, where m is the number of tokens in each cluster. Then, to form a new cluster-level probability distribution $\hat{Y}_C \in \mathcal{R}^n$ ($\sum \hat{Y}_{C,i} = 1$) from the token-level probability distribution \hat{Y} , we employ the following operation to calculate the probability of each cluster, where within a cluster, the samples with larger probability contribute more to the cluster probability:

$$\hat{Y}_{C,j} = \frac{\sum_{i=jm}^{(j+1)m-1} \exp(\hat{Y}_i)}{\sum_{i=1}^N \exp(\hat{Y}_i)}, \quad j = 1, \dots, n \quad (5)$$

where $\hat{Y}_{C,j}$ represents the probability that the generated token belongs to cluster j .

With the ground-truth cluster label y_c and the predicted cluster-level probability distribution $\hat{Y}_{C,i}$, our cluster-oriented cross-entropy loss \mathcal{L}_{CCE} is formulated as:

$$\mathcal{L}_{CCE} = - \sum_{j=1}^n Y_{C,j} \log \hat{Y}_{C,j}, \quad (6)$$

¹After codebook rearrangement, the class label has been updated accordingly.

Type	Model	#Para.	FID↓	IS↑	Precision↑	Recall↑
GAN	BigGAN [5]	112M	6.95	224.5	0.89	0.38
	GigaGAN [23]	569M	3.45	225.5	0.84	0.61
	StyleGAN-XL [37]	166M	2.30	265.1	0.78	0.53
Diffusion	ADM [13]	554M	10.94	101.0	0.69	0.63
	CDM [21]	–	4.88	158.7	–	–
	LDM-4 [35]	400M	3.60	247.7	–	–
	DiT-XL/2 [31]	675M	2.27	278.2	0.83	0.57
Mask.	MaskGIT [7]	227M	6.18	182.1	0.80	0.51
	MaskGIT-re [7]	227M	4.02	355.6	–	–
AR	VQGAN [14]	227M	18.65	80.4	0.78	0.26
	VQGAN [14]	1.4B	15.78	74.3	–	–
	VQGAN-re [14]	1.4B	5.20	280.3	–	–
	ViT-VQGAN [43]	1.7B	4.17	175.1	–	–
	ViT-VQGAN-re [43]	1.7B	3.04	227.4	–	–
	RQTran. [27]	3.8B	7.55	134.0	–	–
	RQTran.-re [27]	3.8B	3.80	323.7	–	–
AR	LlamaGen-B [38]	111M	5.46	193.6	0.83	0.45
	LlamaGen-L [38]	343M	3.29	227.8	0.82	0.53
	LlamaGen-XL [38]	775M	2.63	244.1	0.81	0.58
	LlamaGen-XXL [38]	1.4B	2.34	253.9	0.80	0.59
Ours	IAR-B	111M	5.14	202.0	0.85	0.45
	IAR-L	343M	3.18	234.8	0.82	0.53
	IAR-XL	775M	2.52	248.1	0.82	0.58
	IAR-XXL (CFG=1.7)	1.4B	2.19	278.9	0.81	0.58
	IAR-XXL (CFG=2.5)	1.4B	3.74	362.0	0.86	0.54

Table 1. Comparison between different types of image generation model on class-conditional ImageNet 256×256 benchmark with FID, IS, precision, and recall.

where Y_C is the one-hot vector spanned by the label y_c . With our cluster-oriented loss, even if the model predicts the wrong token index, there is a high probability that the token is located in the target cluster, which ensures a high similarity between the output image and the target one, effectively improving the generation quality and robustness.

Final Loss Function. The final loss function \mathcal{L} combines both the token-oriented cross-entropy loss \mathcal{L}_{TCE} and the cluster-oriented cross-entropy loss \mathcal{L}_{CCE} :

$$\mathcal{L} = \mathcal{L}_{TCE} + \lambda \mathcal{L}_{CCE}. \quad (7)$$

4. Experiments

4.1. Experimental settings

In this paper, we choose LLamaGen [38] as the main baseline and apply our method to it. We follow the official training details and keep the hyperparameters the same as the official ones. We conduct experiments on ImageNet [11]. To evaluate the model performance, we generate 50K images with randomly selected labels. Then, we compute the FID [18], IS [36], precision, and recall [26] for the generated data (see #Suppl for details).

4.2. Comparison Experiments

Comparison with baselines. We compare our model with the GAN-based methods [5, 23, 37], diffusion-based methods [13, 21, 31, 35], mask-prediction-based methods [7] and autoregressive-based methods [14, 27, 38, 43] on ImageNet [11]. The results are shown in Tab. 2. Our method

Tokens	Model	#Para.	50 epoch				300 epoch			
			FID↓	IS↑	Precision↑	Recal↑	FID↓	IS↑	Precision↑	Recal↑
16 × 16	LlamaGen-B	111M	7.22	178.3	0.86	0.38	5.46	193.6	0.84	0.46
	LlamaGen-L	343M	4.20	200.0	0.82	0.51	3.80	248.3	0.83	0.52
	LlamaGen-XL	775M	3.39	227.1	0.81	0.54	-	-	-	-
	LlamaGen-XXL	1.4B	3.09	253.6	0.83	0.53	-	-	-	-
	IAR-B	111M	6.90	179.2	0.86	0.40	5.14	202.0	0.85	0.45
	IAR-L	343M	4.10	207.1	0.82	0.51	3.40	271.3	0.84	0.51
	IAR-XL	775M	3.36	228.9	0.82	0.54	-	-	-	-
	IAR-XXL	1.4B	3.01	257.4	0.83	0.53	-	-	-	-
24 × 24	LlamaGen-B	111M	8.31	154.7	0.84	0.38	6.09	182.5	0.84	0.42
	LlamaGen-L	343M	4.61	191.4	0.82	0.50	3.29	227.8	0.82	0.53
	LlamaGen-XL	775M	3.24	245.7	0.83	0.53	2.63	244.1	0.81	0.58
	LlamaGen-XXL	1.4B	2.89	236.2	0.80	0.56	2.34	253.9	0.81	0.60
	IAR-B	111M	7.80	153.3	0.84	0.39	5.77	192.5	0.85	0.42
	IAR-L	343M	4.35	197.2	0.81	0.51	3.18	234.8	0.82	0.53
	IAR-XL	775M	3.15	228.8	0.81	0.54	2.52	248.1	0.82	0.58
	IAR-XXL	1.4B	2.87	249.9	0.82	0.56	2.19	265.6	0.81	0.58

Table 2. **Comparison with LlamaGen across different image tokens and model sizes.** Following LlamaGen, we only train XL and XXL version on 16×16 tokens for 50 epochs.

achieves the state-of-the-art FID (**2.19**) and IS (**362.0**). And for each model size, our IAR consistently outperforms LlamaGen, demonstrating the effectiveness of our cluster-oriented autoregressive visual generation strategy.

More comparisons with LlamaGen. We further compare our model with the baseline LlamaGen across different model sizes and image tokens to validate the effectiveness of our model. Specifically, we choose four models with model sizes ranging from 111M to 1.4B parameters. And we also conduct experiments on 16×16 image tokens (corresponds to 256×256 image) and 24×24 image tokens (corresponds to 384×384 image). We choose the model trained with 50 epochs and 300 epochs for evaluation. The comparison results are shown in Tab. 2. It can be seen that across different model sizes, image tokens, and training epochs, our model can always improve the baseline with a better FID and IS, validating the effectiveness and robustness of our model in LLM-based visual generation.

Effects of classifier-free guidance (CFG). IAR can employ classifier-free guidance [19] to generate images with higher quality. We show the performance (FID & IS) of our model (111M and 343M parameters) on different CFGs ranging from 1.0 to 2.75 in Fig. 4 (a). It can be seen that compared to the model without CFG (*i.e.*, CFG=1.0), the model with CFG can largely improve the FID, which means the model can generate images with much higher quality. Specifically, as the CFG increases, the FID first decreases and then increases, indicating that a too-large CFG may influence the generation quality, which is consistent with LlamaGen and previous diffusion-based methods [13, 19].

Effects of model size. We conduct experiments on different model sizes, where the parameter number ranges from 111M to 1.4B. It can be seen in Tab. 2 and Fig. 4 (b) that as the parameter number grows, the model shows

a clear improvement in the performance, which aligns with the scaling law [24], indicating that as the number of parameter increases, our IVR can be more effective.

Training efficiency. We compare the training speed between IAR-B and LlamaGen-B (for different model sizes, please refer to #Suppl). We evaluate the model performance on different epochs (from 50 to 300). The FID and IS results are shown in Fig. 4 (c), which shows that our 175-epoch IAR reaches almost the same FID score as the 300-epoch LlamaGen, indicating that our model can accelerate the training speed for almost 42%. And comparing the models trained on 300 epochs, our model effectively improves the generation quality, validating that our model can improve the training efficiency of the LLM-based visual generation model.

4.3. Ablation Study

To evaluate the effectiveness of our model, we conduct several ablation studies to validate each module separately. We conduct the ablation studies based on IAR-B (111M parameters), and train the model for 100 epochs on ImageNet.

Ablation on codebook rearrangement and \mathcal{L}_{CCE} . We first evaluate the effectiveness of the codebook rearrangement strategy and the cluster-oriented cross-entropy loss \mathcal{L}_{CCE} . We conduct experiments on three ablated models: the model without both codebook rearrangement and \mathcal{L}_{CCE} (original LlamaGen), the model without codebook rearrangement, and the model without \mathcal{L}_{CCE} . The results are shown in Tab 3. It can be seen that the model with only the codebook rearrangement (w.o. CCE loss) performs almost the same as LLamaGen. This is because the original token-oriented cross-entropy loss does not consider cluster information and makes no distinction between embeddings with distant indices and those with close indices, thus fail-

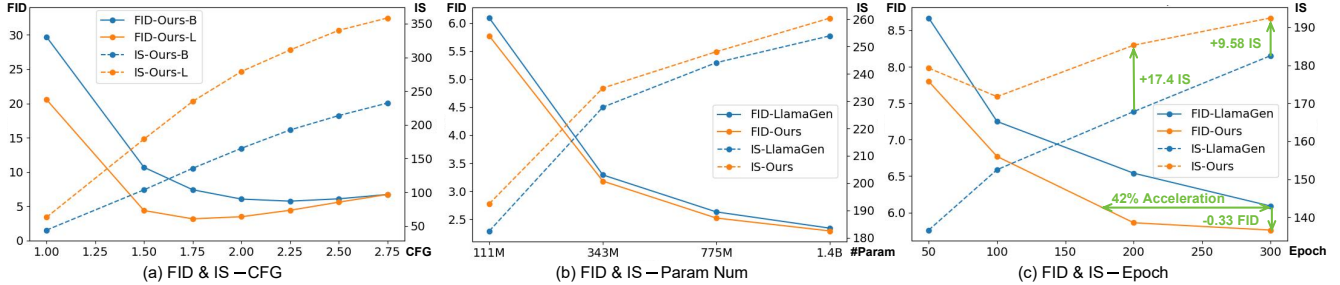


Figure 4. (a) Model performance (IAR-B and IAR-L) across different CFGs; (b) Model performance on different parameter numbers (111M to 3B) compared to LlamaGen; and (c) Model performance on different epochs compared to LlamaGen.

Codebook Rearrangement	\mathcal{L}_{CCE}	FID↓	IS↑	Precision↑	Recall↑
		7.14	166.38	0.84	0.40
✓		7.15	163.09	0.84	0.41
	✓	6.96	168.70	0.84	0.40
✓	✓	6.77	171.73	0.84	0.42

Table 3. Ablation studies on codebook rearrangement strategy and the cluster-oriented cross-entropy loss \mathcal{L}_{CCE} .

ing to utilize the similarity within local clusters. Therefore, even with codebook rearrangement, the result remains almost the same as the original LlamaGen. For the model with CCE loss only (w.o. rearrangement), we treat adjacent embeddings in a window (*e.g.*, 0-128-th codes, 128-256-th codes) as a “cluster”. Without the clustering and reordering process, codes in such “clusters” are not similar to each other, therefore CCE loss cannot function well and only slightly improves the performance. In contrast, our model with both codebook rearrangement and \mathcal{L}_{CCE} has the best performance in fitting the ImageNet dataset.

Ablation on cluster size. A key hyperparameter in our model is the size of each cluster. A too-small cluster size may make it too hard for the model to predict the correct cluster index, which leads the model to perform similarly to the original LlamaGen (Note that the model with cluster size 1 is the same as LlamaGen). In contrast, a too-big cluster size may cause the image embeddings in each cluster to be too different, such that even if the model predicts the correct cluster index, the gap to the target image embedding is still too big. Therefore, it is important to choose an appropriate cluster size to balance the inner similarity in each cluster and the ease of predicting the correct cluster index. We conduct experiments on different cluster sizes ranging from 1 to 512, where the codebook size is 16384. We compute the inner MSE of cluster, *i.e.*, the average distance from each code in a cluster to the centroid, and evaluate the model performance by FID, IS, Precision, and Recall in Tab. 4. It can be seen that as the cluster size increases, the inner MSE distance becomes higher, indicating that the image codes in each cluster become less similar. Moreover, the model reaches the best performance when the cluster size is 128, which happens to be the square root of the codebook size.

Cluster Size	Inner MSE	FID↓	IS↑	Precision↑	Recall↑
1	0	7.14	166.38	0.84	0.40
8	0.018	7.02	167.09	0.85	0.40
16	0.022	6.99	166.39	0.84	0.42
32	0.028	6.83	170.10	0.84	0.40
64	0.034	6.92	171.65	0.85	0.39
128	0.041	6.77	171.73	0.84	0.42
256	0.050	6.81	170.58	0.85	0.41
512	0.059	6.94	163.54	0.83	0.42

Table 4. Ablation studies on different cluster sizes from 1 to 512, where cluster size 1 corresponds to the official LlamaGen.

λ	FID↓	IS↑	Precision↑	Recall↑
0	7.14	166.38	0.84	0.40
0.1	7.01	167.16	0.84	0.40
0.25	7.05	160.73	0.84	0.42
0.5	6.78	171.15	0.84	0.41
0.75	6.80	170.06	0.84	0.41
1	6.77	171.73	0.84	0.42
1.5	6.87	170.60	0.84	0.41

Table 5. Ablation studies on the weight λ of the cluster-oriented cross-attention loss \mathcal{L}_{CCE} .

Ablation on weight of \mathcal{L}_{CCE} . Since we introduce an additional cluster-oriented cross-entropy loss \mathcal{L}_{CCE} during the training process, we conduct experiments to find the influence of its corresponding weight λ . We choose λ ranging from 0.1 to 1.5 and evaluate the model performance in Tab. 5. It can be seen that a too-small weight will cause the model to perform similarly to the original LlamaGen, while a too-big weight will make the model concern too much about the cluster index and overlook the ground-truth token index, which also makes the model perform worse. In summary, we find that when the weight $\lambda = 1$, the model can balance the two goals and achieves the best performance.

5. Conclusion

In this paper, we analyzed the difference between the natural language and images in LLM-based visual generation. We find that similar image embeddings in the codebook can produce similar images. Based on this observation, we propose IAR, an Improved Autoregressive Visual Generation

Method that effectively enhances the training efficiency and quality of the LLM-based visual generation model. We first conduct Codebook Rearrangement with a balanced K-means clustering algorithm to reorder the codebook into clusters with equal sizes, where the image embeddings within each cluster share similarities. Then, we introduce a Cluster-oriented Cross-entropy Loss to enable the model to learn the target cluster, which can guarantee a good generation quality even if the model predicts a wrong image token. We validate the effectiveness of our IAR on LlamaGen, and find that IAR can largely improve the training efficiency and generation quality across different parameter scales. Moreover, our IAR can be seamlessly applied to various LLM-based visual generation model, pointing out a new direction to improve the LLM-based visual generation field.

References

- [1] Josh Achiam, Steven Adler, Sandhini Agarwal, Lama Ahmad, Ilge Akkaya, Florencia Leoni Aleman, Diogo Almeida, Janko Altmenschmidt, Sam Altman, Shyamal Anadkat, et al. Gpt-4 technical report. *arXiv preprint arXiv:2303.08774*, 2023. 3
- [2] David H. Ackley, Geoffrey E. Hinton, and Terrence J. Sejnowski. A learning algorithm for boltzmann machines. *Cognitive Science*, 1985. 11
- [3] Jinbin Bai, Tian Ye, Wei Chow, Enxin Song, Qing-Guo Chen, Xiangtai Li, Zhen Dong, Lei Zhu, and Shuicheng Yan. Meissonic: Revitalizing masked generative transformers for efficient high-resolution text-to-image synthesis. *arXiv preprint arXiv:2410.08261*, 2024. 1, 3
- [4] Andreas Blattmann, Tim Dockhorn, Sumith Kulal, Daniel Mendelevitch, Maciej Kilian, Dominik Lorenz, Yam Levi, Zion English, Vikram Voleti, Adam Letts, et al. Stable video diffusion: Scaling latent video diffusion models to large datasets. *arXiv preprint arXiv:2311.15127*, 2023. 1, 3
- [5] Andrew Brock, Jeff Donahue, and Karen Simonyan. Large scale gan training for high fidelity natural image synthesis. *arXiv preprint arXiv:1809.11096*, 2018. 6
- [6] Tom B Brown. Language models are few-shot learners. *arXiv preprint arXiv:2005.14165*, 2020. 3
- [7] Huiwen Chang, Han Zhang, Lu Jiang, Ce Liu, and William T Freeman. Maskgit: Masked generative image transformer. In *CVPR*, 2022. 1, 3, 6
- [8] Huiwen Chang, Han Zhang, Jarred Barber, Aaron Maschinot, Jose Lezama, Lu Jiang, Ming-Hsuan Yang, Kevin Patrick Murphy, William T. Freeman, Michael Rubinstein, Yuanzhen Li, and Dilip Krishnan. Muse: Text-to-image generation via masked generative transformers. In *Proceedings of the 40th International Conference on Machine Learning*, 2023. 3
- [9] Aakanksha Chowdhery, Sharan Narang, Jacob Devlin, Maarten Bosma, Gaurav Mishra, Adam Roberts, Paul Barham, Hyung Won Chung, Charles Sutton, Sebastian Gehrmann, et al. Palm: Scaling language modeling with pathways. *JMLR*, 2023. 3
- [10] Kevin Clark, Minh-Thang Luong, Quoc V. Le, and Christopher D. Manning. ELECTRA: Pre-training text encoders as discriminators rather than generators. In *ICLR*, 2020. 3
- [11] Jia Deng, Wei Dong, Richard Socher, Li-Jia Li, Kai Li, and Li Fei-Fei. Imagenet: A large-scale hierarchical image database. In *CVPR*, 2009. 6, 12, 13, 14
- [12] Jacob Devlin. Bert: Pre-training of deep bidirectional transformers for language understanding. *arXiv preprint arXiv:1810.04805*, 2018. 2, 3
- [13] Prafulla Dhariwal and Alexander Nichol. Diffusion models beat gans on image synthesis. In *NeurIPS*, 2021. 3, 6, 7
- [14] Patrick Esser, Robin Rombach, and Bjorn Ommer. Taming transformers for high-resolution image synthesis. In *CVPR*, 2021. 2, 3, 4, 5, 6
- [15] Patrick Esser, Sumith Kulal, Andreas Blattmann, Rahim Entezari, Jonas Müller, Harry Saini, Yam Levi, Dominik Lorenz, Axel Sauer, Frederic Boesel, et al. Scaling rectified flow transformers for high-resolution image synthesis. In *ICML*, 2024. 3
- [16] Ian Goodfellow, Jean Pouget-Abadie, Mehdi Mirza, Bing Xu, David Warde-Farley, Sherjil Ozair, Aaron Courville, and Yoshua Bengio. Generative adversarial networks. *Commun Acn*, 2020. 1, 3
- [17] Yuwei Guo, Ceyuan Yang, Anyi Rao, Zhengyang Liang, Yaohui Wang, Yu Qiao, Maneesh Agrawala, Dahua Lin, and Bo Dai. Animatediff: Animate your personalized text-to-image diffusion models without specific tuning. In *ICLR*, 2024. 1, 3
- [18] Martin Heusel, Hubert Ramsauer, Thomas Unterthiner, Bernhard Nessler, and Sepp Hochreiter. Gans trained by a two time-scale update rule converge to a local nash equilibrium. In *NeurIPS*, 2017. 6, 11
- [19] Jonathan Ho and Tim Salimans. Classifier-free diffusion guidance. *arXiv preprint arXiv:2207.12598*, 2022. 7, 11
- [20] Jonathan Ho, Ajay Jain, and Pieter Abbeel. Denoising diffusion probabilistic models. In *NeurIPS*, 2020. 1, 3
- [21] Jonathan Ho, Chitwan Saharia, William Chan, David J Fleet, Mohammad Norouzi, and Tim Salimans. Cascaded diffusion models for high fidelity image generation. *JMLR*, 2022. 3, 6
- [22] Ari Holtzman, Jan Buys, Li Du, Maxwell Forbes, and Yejin Choi. The curious case of neural text degeneration. In *ICLR*, 2019. 11
- [23] Minguk Kang, Jun-Yan Zhu, Richard Zhang, Jaesik Park, Eli Shechtman, Sylvain Paris, and Taesung Park. Scaling up gans for text-to-image synthesis. In *CVPR*, 2023. 6
- [24] Jared Kaplan, Sam McCandlish, Tom Henighan, Tom B Brown, Benjamin Chess, Rewon Child, Scott Gray, Alec Radford, Jeffrey Wu, and Dario Amodei. Scaling laws for neural language models. *arXiv preprint arXiv:2001.08361*, 2020. 7, 13
- [25] Tero Karras, Samuli Laine, and Timo Aila. A style-based generator architecture for generative adversarial networks. In *CVPR*, 2019. 3
- [26] Tuomas Kynkäänniemi, Tero Karras, Samuli Laine, Jaakko Lehtinen, and Timo Aila. Improved precision and recall metric for assessing generative models. In *NeurIPS*, 2019. 6, 11

- [27] Doyup Lee, Chiheon Kim, Saehoon Kim, Minsu Cho, and Wook-Shin Han. Autoregressive image generation using residual quantization. In *CVPR*, 2022. 6
- [28] Yinhan Liu. Roberta: A robustly optimized bert pretraining approach. *arXiv preprint arXiv:1907.11692*, 2019. 3
- [29] Enrique Manjavacas, Folgert Karsdorp, Ben Burtenshaw, and Mike Kestemont. Synthetic literature: Writing science fiction in a co-creative process. In *CCNLG*, 2017. 11
- [30] Shervin Minaee, Tomas Mikolov, Narjes Nikzad, Meysam Chenaghlu, Richard Socher, Xavier Amatriain, and Jianfeng Gao. Large language models: A survey. *arXiv preprint arXiv:2402.06196*, 2024. 3
- [31] William Peebles and Saining Xie. Scalable diffusion models with transformers. In *ICCV*, 2023. 3, 6
- [32] Andrea Pietracaprina, Matteo Riondato, Eli Upfal, and Fabio Vandin. Mining top-k frequent itemsets through progressive sampling. *DATAMINE*, 2010. 11
- [33] Alec Radford. Improving language understanding by generative pre-training. 2018. 3
- [34] Alec Radford, Jeffrey Wu, Rewon Child, David Luan, Dario Amodei, Ilya Sutskever, et al. Language models are unsupervised multitask learners. *OpenAI blog*, 2019. 1, 2, 3
- [35] Robin Rombach, Andreas Blattmann, Dominik Lorenz, Patrick Esser, and Björn Ommer. High-resolution image synthesis with latent diffusion models. In *CVPR*, 2022. 1, 3, 6
- [36] Tim Salimans, Ian Goodfellow, Wojciech Zaremba, Vicki Cheung, Alec Radford, and Xi Chen. Improved techniques for training gans. In *NeurIPS*, 2016. 6, 11
- [37] Axel Sauer, Katja Schwarz, and Andreas Geiger. Stylegan-xl: Scaling stylegan to large diverse datasets. In *ACM SIGGRAPH*, 2022. 6
- [38] Peize Sun, Yi Jiang, Shoufa Chen, Shilong Zhang, Bingyue Peng, Ping Luo, and Zehuan Yuan. Autoregressive model beats diffusion: Llama for scalable image generation. *arXiv preprint arXiv:2406.06525*, 2024. 1, 2, 3, 5, 6, 11, 13, 14, 15
- [39] Chameleon Team. Chameleon: Mixed-modal early-fusion foundation models. *arXiv preprint arXiv:2405.09818*, 2024. 1
- [40] Keyu Tian, Yi Jiang, Zehuan Yuan, Bingyue Peng, and Liwei Wang. Visual autoregressive modeling: Scalable image generation via next-scale prediction. In *NeurIPS*, 2024. 1, 3, 5, 11, 12, 13
- [41] Hugo Touvron, Thibaut Lavril, Gautier Izacard, Xavier Martinet, Marie-Anne Lachaux, Timothée Lacroix, Baptiste Rozière, Naman Goyal, Eric Hambro, Faisal Azhar, et al. Llama: Open and efficient foundation language models. *arXiv preprint arXiv:2302.13971*, 2023. 3
- [42] Jinbo Xing, Menghan Xia, Yong Zhang, Haoxin Chen, Wangbo Yu, Hanyuan Liu, Gongye Liu, Xintao Wang, Ying Shan, and Tien-Tsin Wong. Dynamicrafter: Animating open-domain images with video diffusion priors. In *ECCV*, 2025. 3
- [43] Jiahui Yu, Xin Li, Jing Yu Koh, Han Zhang, Ruoming Pang, James Qin, Alexander Ku, Yuanzhong Xu, Jason Baldridge, and Yonghui Wu. Vector-quantized image modeling with improved vqgan. In *ICLR*, 2021. 3, 6
- [44] Richard Zhang, Phillip Isola, Alexei A Efros, Eli Shechtman, and Oliver Wang. The unreasonable effectiveness of deep features as a perceptual metric. In *CVPR*, 2018. 4
- [45] Chunting Zhou, Lili Yu, Arun Babu, Kushal Tirumala, Michihiro Yasunaga, Leonid Shamis, Jacob Kahn, Xuezhe Ma, Luke Zettlemoyer, and Omer Levy. Transfusion: Predict the next token and diffuse images with one multi-modal model. *arXiv preprint arXiv:2408.11039*, 2024. 1

A. Overview

The supplementary material is composed of:

- Implementation details (Sec. B);
- More details on optimization relaxation in codebook rearrangement (Sec. C)
- Comparison with VAR [40] (Sec. D)
- More analysis on our model (Sec. E);
- More visualization results (Sec. F);
- Future work (Sec. G).

We also provide the code of our model in the supplementary material, which can be easily applied to the existing autoregressive models.

B. Implementation Details

Metrics. We employ four metrics to evaluate the effectiveness of the models:

- **Fréchet inception distance (FID)** [18] measures the similarity between the features of the source data and the generated data according to their mean values and covariance. A smaller FID indicates better generation ability.
- **Inception Score (IS)** [36] measures the quality and diversity of images by computing the information entropy of the generated images. A higher IS indicates better generation quality and diversity.
- **Precision/Recall** [26] measures the class-conditional generation accuracy. A higher precision or recall indicates a better class-conditional generation performance.

Experiment settings. We follow the experiment settings as LlamaGen [38] and keep the hyperparameters consistent with it. The experiment details are shown in Tab. A1 and Tab. A2, where Tab. A2 is the inference settings for Tab. 2 of the main paper.

Sampling hyperparameters: Among the hyperparameters used in the inference process (Tab. A2), there are several important parameters, whose meanings are explained in detail below:

(1) Classifier-free guidance: Classifier-Free Guidance (CFG) [19] is originally a sampling method to improve diffusion models by combining conditional and unconditional score estimates. Beyond diffusion models, CFG can also be applied to the autoregressive image generation process [38]. Denoting the input image token sequence as q , our model as ϵ_θ , and the class condition as c , the autoregressive CFG is defined as:

$$\tilde{\epsilon}_\theta(q, c) = (1 + w)\epsilon_\theta(q, c) - w\epsilon_\theta(q, \phi), \quad (\text{A1})$$

where ϕ denotes the empty condition and $\epsilon(\cdot, \cdot)$ represents the predicted probability distribution for the next image token.

(2) Top-K: Top-K sampling [32] is a decoding strategy that selects tokens from the top k highest-probability candidates. It focuses on the most likely tokens, but the fixed k size may exclude important low-probability options.

(3) Top-P: Top-P sampling [22], also known as nucleus sampling, selects tokens dynamically from the smallest set whose cumulative probability meets or exceeds a threshold p . This approach adapts to the output distribution, balancing coherence and diversity in text generation.

(4) Temperature: In large language models (LLMs), temperature [2, 29] is a hyperparameter that controls the randomness of the generated token by adjusting the sharpness of the probability distribution: lower values make the output more deterministic, while higher values increase diversity and randomness. The probability P_i for each token is calculated as:

$$P_i = \frac{\exp(l_i/T)}{\sum_j \exp(l_j/T)},$$

where l_i represents the predicted probability distribution, and T is the temperature.

C. Complexity Analysis of Codebook Rearrangement Target

In Sec. 3.2 of the main paper, we aim to rearrange the codebook such that the neighboring embeddings are as close to each other. We summarize this code rearrangement problem as an optimization problem, where we aim to find a surjective mapping $M(\cdot)$ that satisfies:

$$M = \arg \min_M \sum_{i=1}^{N-1} \|z_{M(i)}, z_{M(i+1)}\|. \quad (\text{A2})$$

After reordering each embedding z_i to index $M(i)$, the sum of distances between adjacent embeddings is minimized. And $\hat{\mathcal{Z}} = M(\mathcal{Z})$ is the rearranged codebook.

However, this optimization can be reduced to the Shortest Hamiltonian path problem, which is a classical NP-hard problem. The Shortest Hamiltonian Path Problem is a variation of the Hamiltonian Path Problem. Its goal is to find a path that visits each vertex exactly once and minimizes the total weight (or distance) of the path. Formally, given a weighted graph $G = (V, E)$ with a weight function $w : E \rightarrow \mathbb{R}^+$, the goal is to find a Hamiltonian path $\pi^* = (\pi_1, \pi_2, \dots, \pi_N)$ such that the sum of the weights of the edges in the path, *i.e.*, $\sum_{i=1}^{N-1} w(\pi_i, \pi_{i+1})$, is minimized, which is formulated as:

$$\pi^* = \arg \min_\pi \sum_{i=1}^{N-1} w(\pi_i, \pi_{i+1}). \quad (\text{A3})$$

Next, we prove that solving the optimization problem in Eq. (A2) can be reduced to the Shortest Hamiltonian path problem in Eq. (A3):

Proposition: Solving Eq. (A3) \leq_p Solving Eq. (A2)

Proof.

Model	B	L	XL	XXL	B	L	XL	XXL
Parameter Num	111M	343M	775M	1.4B	111M	343M	775M	1.4B
Token Num	16×16				24×24			
Optimizer	AdamW							
Weight decay	0.05							
Learning Rate Scheduler	Constant							
Batch Size	256	256	256	256	256	256	256	512
Learning Rate	1E-04	1E-04	2E-04	2E-04	1E-04	1E-04	2E-04	2E-04
GPU Num	8	8	8	8	8	8	16	32
Epoch	300	300	50	50	300	300	300	300
FSDP	No	No	No	Yes	No	No	No	Yes

Table A1. The training settings and hyperparameters used in our model.

Model	B	L	XL	XXL	B	L	XL	XXL
Parameter Num	111M	343M	775M	1.4B	111M	343M	775M	1.4B
Token Num	16×16				24×24			
Batch Size					32			
Random Seed					0			
Top K					0			
Top P					1.0			
Temperature					1.0			
CFG	2.0	2.0	1.75	2.0	2.25	1.75	1.75	1.65

Table A2. The inference settings and hyperparameters used in Tab. 2 of the main paper.

Step 1: Construct a Complete Weighted Graph:

Define a complete graph $G = (V, E)$ where the vertex set $V = \{0, 1, \dots, N - 1\}$ corresponds to the N embeddings in the codebook \mathcal{Z} . Each edge $(i, j) \in E$ is assigned a weight $w(i, j)$ that equals to the distance between embeddings z_i and z_j :

$$w(i, j) = \|z_i, z_j\|. \quad (\text{A4})$$

Step 2: Find the Minimum Weight Hamiltonian Path:

Finding the shortest Hamiltonian path $\pi = (\pi_1, \pi_2, \dots, \pi_N)$ in G aims to minimize the total weight:

$$\pi^* = \arg \min_{\pi} \sum_{i=1}^{N-1} w(\pi_i, \pi_{i+1}). \quad (\text{A5})$$

Step 3: Mapping to the Original Problem:

The shortest Hamiltonian path π^* provides the optimal permutation M^* for the optimization problem in Eq. (A2), where $M^*(i) = \pi_i$, for $i = 1, 2, \dots, N$.

In summary, the original optimization problem (in Eq. (A2)) of finding the optimal surjective mapping $M(\cdot)$ to minimize the sum of distances between consecutive embeddings, can be reduced to finding the minimum weight

Hamiltonian path in a complete weighted graph, where the weights are given by the distances between embeddings.

Therefore, the original optimization problem is also NP-hard. And it is necessary to relax this optimization target to a clustering problem (main paper Sec. 3.2), which ensures the embeddings with a cluster share high similarities.

D. Comparing IAR+VAR with VAR

VAR [40] extends the next-token prediction in autoregressive image generation to next-scale prediction, enabling the model to generate images progressively from small to large scales. At each scale, VAR predicts all tokens simultaneously, significantly enhancing the inference speed of the autoregressive image generation process. Our design is independent of the model structure in autoregressive image generation, allowing us to integrate our IAR with VAR, referred to as VAR+IAR. Given that most official VAR models are trained on 256 A100 GPUs, which is highly resource-intensive, we only train the VAR-d16 model for 100 epochs on ImageNet [11] and subsequently compare it with VAR+IAR.

Both models (VAR and VAR+IAR) are trained for 100

Classifier-free Guidance	VAR-d16 + IAR				VAR-d16			
	FID↓	IS↑	Precision↑	Recall↑	FID↓	IS↑	Precision↑	Recall↑
1.5	4.12	58.15	0.839	0.482	4.28	56.66	0.830	0.479
1.75	4.07	60.54	0.857	0.458	4.25	59.00	0.846	0.460
2.0	4.43	63.11	0.865	0.435	4.52	61.00	0.860	0.435

Table A3. Comparing VAR-d16 [40] with VAR+IAR on ImageNet [11]. It shows that our IAR also performs well in the next-scale prediction model, validating that our method can be widely applied to various autoregressive image generation models, enhancing their generative capabilities.

Classifier-free Guidance	IAR-B				IAR-L			
	FID↓	IS↑	Precision↑	Recall↑	FID↓	IS↑	Precision↑	Recall↑
1	29.70	43.96	0.566	0.632	20.56	62.96	0.595	0.666
1.5	10.69	103.59	0.732	0.532	4.39	178.78	0.778	0.566
1.75	7.43	135.55	0.783	0.501	3.18	234.79	0.824	0.530
2	6.06	165.22	0.822	0.454	3.49	279.09	0.855	0.499
2.25	5.77	192.45	0.850	0.421	4.43	311.08	0.873	0.466
2.5	6.11	213.76	0.869	0.381	5.61	340.18	0.890	0.425
2.75	6.73	232.35	0.884	0.360	6.74	358.48	0.898	0.401

Table A4. The Quantitative metrics on our model under different classifier-free guidance scales.

epochs with a batch size of 768, maintaining the same hyperparameters as the official VAR code. We then evaluate the trained models on different CFGs. The results, presented in Tab. A3, demonstrate that incorporating IAR into VAR enhances the original VAR in terms of generation quality and diversity, as evidenced by improved FID and IS scores. This validates the effectiveness of our model across different autoregressive image generation frameworks, showing the great potential of our IAR in the field of autoregressive image generation.

E. More Analysis on Our Model

Comprehensive metrics for models under different CFGs. This section presents the comprehensive metrics (FID, IS, Precision, Recall) for the models compared in Fig. 4 (a) of the main paper. As shown in Table A4, an increase in CFG leads to higher IS and precision, while recall decreases. Unlike these three metrics, FID initially improves and then deteriorates, achieving its optimal value at an intermediate CFG. Furthermore, the optimal CFG for FID varies with model size (e.g., CFG=2.25 for IAR-B and CFG=1.75 for IAR-L).

Comprehensive metrics for models under different training epochs. Table A5 presents a comparison between our IAR and LlamaGen [38] over various training epochs, illustrating that our model consistently outperforms LlamaGen at all stages of training. Notably, the 200-epoch IAR-B exceeds the performance of the 300-epoch LlamaGen-B, while the 200-epoch IAR-L performs similarly to the

300-epoch LlamaGen-L, highlighting the high training efficiency of our model. (Note that all B-version models use CFG=2.25, whereas all L-version models use CFG=1.75)

Training losses for different model sizes. We show the training loss curves for both the two losses: 1) cluster-oriented cross-entropy loss \mathcal{L}_{CCE} and the token-oriented cross-entropy loss \mathcal{L}_{TCE} when training on 24×24 image tokens (Fig. A1) and 16×16 image tokens (Fig. A2). It can be seen that as the model size increases, both the two losses decrease faster and converge to a lower value, which aligns with the scaling law [24]. Note that since we follow the training setting of LlamaGen [38], we only train IAR-XL and IAR-XXL on 16×16 image tokens for 50 epochs.

Effectiveness of \mathcal{L}_{CCE} . In the main paper, we introduce the cluster-oriented cross-entropy loss \mathcal{L}_{CCE} , designed to enhance the model’s awareness of cluster information, thereby increasing the likelihood of predicting tokens within the target cluster. It is hard to directly illustrate the effectiveness of \mathcal{L}_{CCE} by its loss value directly. Therefore, we design an alternative way where we visualize the loss curves for token-oriented cross-entropy loss \mathcal{L}_{TCE} and their corresponding FIDs for LlamaGen-B and our model in Fig. A3. The results indicate that, compared to LlamaGen, our model exhibits a higher token-oriented cross-entropy loss but achieves a superior FID. This suggests that our model has slightly lower token-oriented prediction accuracy, which is expected since the introduction of \mathcal{L}_{CCE} partially diverts the original loss \mathcal{L}_{TCE} . Therefore, the improvement of FID can only come from our proposed cluster-oriented cross-entropy loss \mathcal{L}_{CCE} . Since \mathcal{L}_{CCE} ef-

Model Size	Epoch	LlamaGen				IAR			
		FID↓	IS↑	Precision↑	Recall↑	FID↓	IS↑	Precision↑	Recall↑
B Version	50	8.67	136.62	0.818	0.413	7.80	153.31	0.839	0.394
	100	7.26	152.50	0.827	0.416	6.77	171.73	0.839	0.416
	200	6.54	167.82	0.833	0.428	5.86	185.28	0.845	0.428
	300	6.09	182.54	0.845	0.416	5.77	192.45	0.850	0.421
L Version	50	4.25	191.46	0.819	0.504	4.35	197.23	0.819	0.507
	100	3.96	199.96	0.803	0.532	3.81	205.63	0.805	0.528
	200	3.33	219.57	0.804	0.538	3.31	225.95	0.814	0.551
	300	3.29	227.83	0.818	0.532	3.18	234.79	0.824	0.530

Table A5. The Quantitative metrics on our model and LlamaGen under different training epochs. The B version employs CFG=2.25 and the L-version employs CFG=1.75.

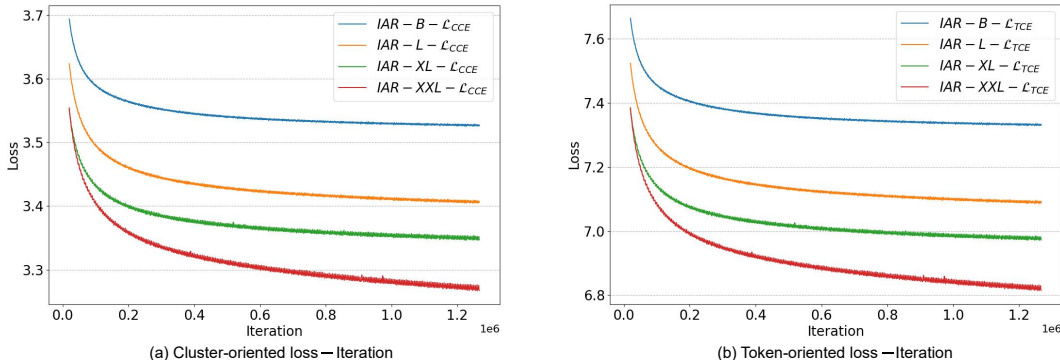


Figure A1. The training loss curves for the cluster-oriented cross-entropy loss \mathcal{L}_{CCE} (a) and token-oriented cross-entropy loss \mathcal{L}_{TCE} (b) on 24×24 image tokens.

fectively increases the likelihood of predicting the correct cluster, combined with the embedding similarities within the cluster, it ultimately leads to the generation of images with better FID, demonstrating the efficacy of \mathcal{L}_{CCE} in our model.

Token prediction accuracy. We compute the token prediction accuracy of our model and LlamaGen [38] on different model sizes (24×24 tokens). Specifically, for an image token sequence $q = \{q^1, q^2, \dots, q^{576}\}$ with corresponding image embedding sequence $z_q = \{z_q^1, z_q^2, \dots, z_q^{576}\}$ and class label c , we enumerate i from 1 to 575 and predict $\hat{q}^{i+1} \sim P^{i+1} = \epsilon_\theta(\hat{q}^{i+1}|c, q^1, q^2, \dots, q^i)$ using the model ϵ_θ . We then compute the Top-1 and Top-5 accuracy Acc^i between \hat{q}^{i+1} and the ground truth q^{i+1} . The average accuracy for an image is calculated as $Acc = \frac{1}{575} \sum_{i=1}^{575} Acc^i$. Finally, we compute the cluster-level accuracy and token-level accuracy for all images in ImageNet [11] and record the average values in Tab. A6. Specifically, to compute the cluster-level accuracy for LlamaGen, we employ the balanced K-means clustering algorithm to decompose the codebook into n clusters and then determine the target cluster index. We then assess whether the predicted token is located in the target cluster, thereby obtaining the cluster-level accuracy. From Tab. A6, it can be seen that our cluster-

level accuracy is higher than that of LlamaGen, indicating the effectiveness of our cluster-oriented cross-entropy loss \mathcal{L}_{CCE} . Although our token-level accuracy is slightly lower, this is expected as the newly included loss \mathcal{L}_{CCE} affects the original token-oriented cross-entropy loss \mathcal{L}_{TCE} , resulting in a slight decrease in token-level accuracy. However, our model still achieves better FID and IS compared to LlamaGen, further validating the effectiveness of our cluster-oriented token prediction strategy.

F. More Visualization Results

We exhibit more generated images from our model in Fig. A4~A7, where the images are generated by The XXL-version with 4.0 CFG, with image size 384×384 . We show 16 classes of images, including alp, promontory, volcano, coral reef, sports car, balloon, convertible, space shuttle, castle, church, beacon, cinema, bridge, ocean liner, white stork, and Pomeranian.

G. Future Work

The main idea of our IAR is to ensure a high similarity between the predicted image embedding and the target embedding, so that even if the model incorrectly predicts the

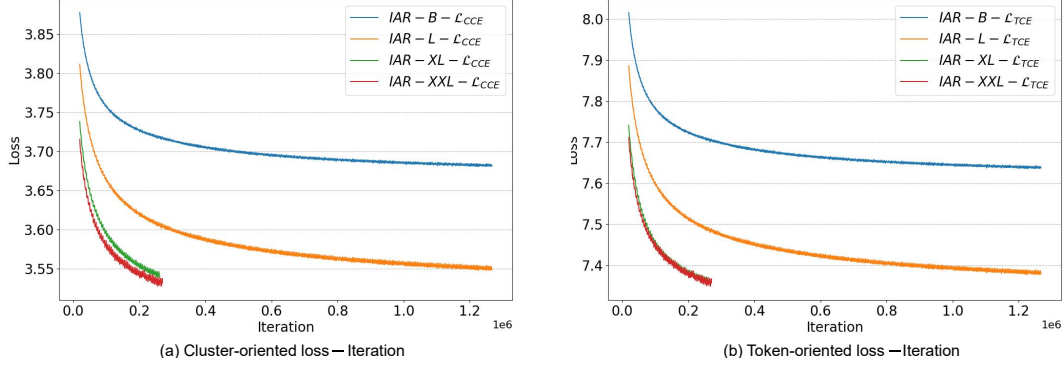


Figure A2. The training loss curves for the cluster-oriented cross-entropy loss \mathcal{L}_{CCE} (a) and token-oriented cross-entropy loss \mathcal{L}_{TCE} (b) on 16×16 image tokens.

Model	IAR				LlamaGen [38]			
	B	L	XL	XXL	B	L	XL	XXL
Cluster-level Accuracy (Top-1, %)	15.54	17.12	18.01	19.02	13.44	14.81	15.71	16.49
Cluster-level Accuracy (Top-5, %)	41.48	44.68	46.30	48.29	30.37	33.13	34.87	36.38
Token-level Accuracy (Top-1, %)	2.62	3.17	3.56	3.88	2.64	3.19	3.59	3.95
Token-level Accuracy (Top-5, %)	7.34	8.86	9.90	10.75	7.37	8.91	9.98	10.96

Table A6. Comparison of the token-level prediction accuracy, cluster-level prediction accuracy, and the embedding-level MSE distance between our IAR and LlamaGen.

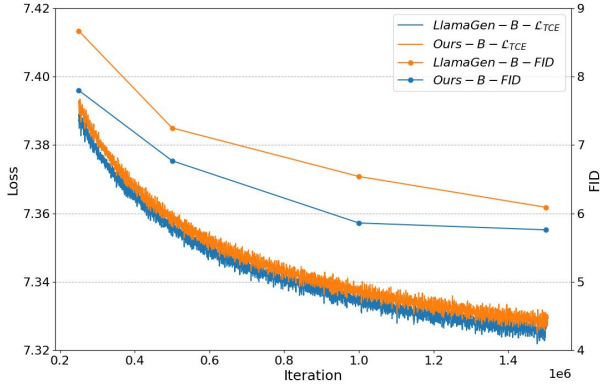


Figure A3. Comparison between LlamaGen-B and ours on the **token-oriented cross-entropy loss** \mathcal{L}_{TCE} and the **FID** score in different training iterations. Our model has a higher \mathcal{L}_{TCE} than that of LlamaGen but achieves a better FID, indicating the effectiveness of our cluster-oriented cross-entropy loss \mathcal{L}_{CCE} .

target token, the output image still closely resembles the target image. This can be naturally considered as a continuous constraint on the image embedding, aiming to minimize the distance between the predicted and target image embeddings. However, this approach cannot be easily applied to LLM-based image generation models due to the non-differentiable nature of the embedding quantization operation. Therefore, this paper relaxes the problem into a cluster-oriented token prediction problem, which can be easily integrated into the current autoregressive image gen-

eration model. We believe that in future work, employing this continuous constraint in autoregressive image generation may further enhance the model performance.



Figure A4. The generated images for alp, promontory, volcano, and coral reef by IAR-XXL with 4.0 CFG.



Figure A5. The generated images for sports car, balloon, convertible, and space shuttle by IAR-XXL with 4.0 CFG.

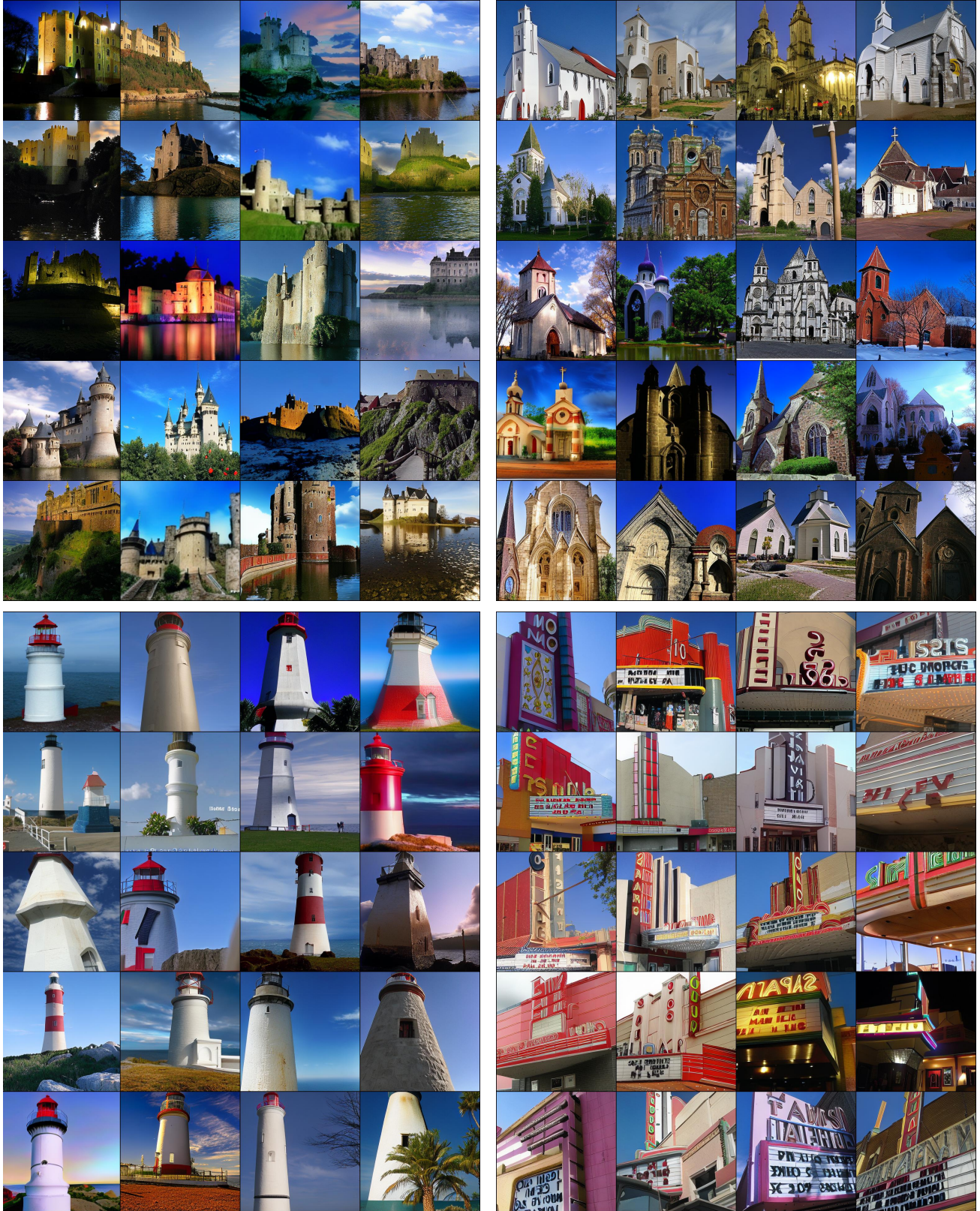


Figure A6. The generated images for castle, church, beacon, and cinema by IAR-XXL with 4.0 CFG.

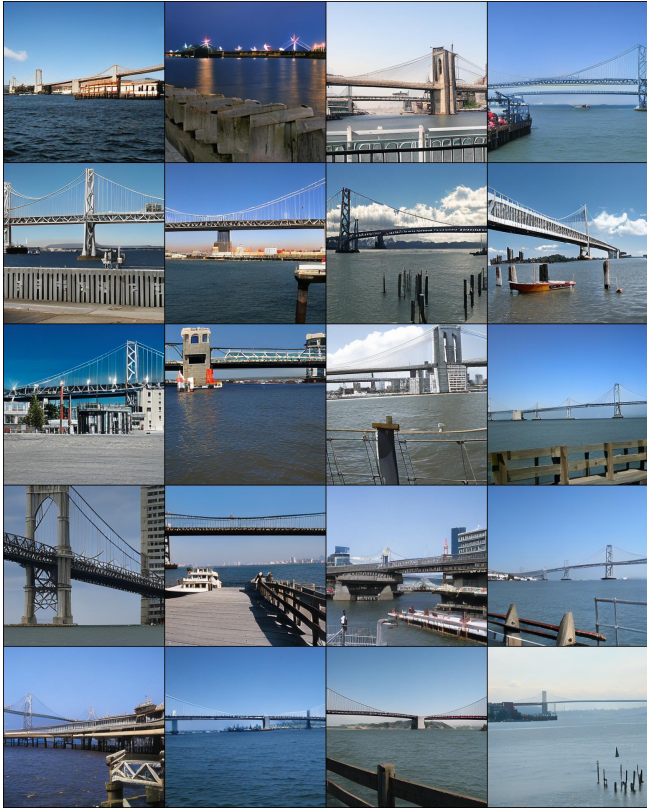


Figure A7. The generated images for bridge, ocean liner, white stork, and Pomeranian by IAR-XXL with 4.0 CFG.